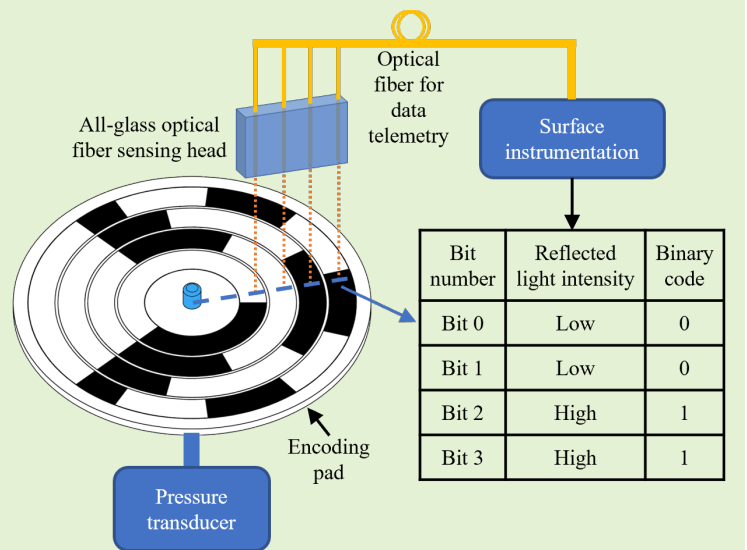**IEEE Sensors Council**

Glass Additive and Subtractive Manufacturing of a Fiber Optic Rotary Encoder for Downhole Pressure Sensing

Xuran Zhu, Jianan Tang, Yongji Wu, Xinyu Jiao, Runar Nygaard, David Cercone, Hai Xiao

Abstract— This paper presents a fiber optic rotary encoder-based pressure sensor for downhole applications. The rotary encoder, which is composed of an encoding pad and an all-glass optical fiber sensing head, converts the rotation angles of a pressure transducer to digital codes. The optical fiber only serves as the telemetry channel to directly transmit the data in digital format, such that the environmental temperature influence and the long-time drift are minimized. The glass additive and subtractive manufacturing techniques are used to embed the multi-channel optical fibers into a bulk-fused silica glass substrate. Because the fused silica glass shares a similar material property to the optical fiber (e.g., thermal expansion coefficient), the optical fiber sensing head is well sealed and fixed even at an elevated temperature. The picosecond laser blackening technique is used to fabricate the high reflectivity contrast encoding pad with high accuracy. The proposed pressure sensor was manufactured and experimentally verified to have a signal-to-noise ratio of 23 dB and a linear pressure response with a root-mean-square error of 0.37. During the 400-hour 250°C long-term stability test, there was no digital code variation. In addition, a mathematical model to study the relationships between the sensor's performances and design parameters were established. According to the model, a 12-bit encoder (0.02% pressure sensitivity) can be achieved with a radius of 20 mm.

Bit number	Reflected light intensity	Binary code
Bit 0	Low	0
Bit 1	Low	0
Bit 2	High	1
Bit 3	High	1

Index Terms—Downhole pressure sensing, fiber optic rotary encoder, glass additive manufacturing, fiber optic sensor

I. INTRODUCTION

DOWNHOLE pressure monitoring in the oil and gas industry plays an important role in oil exploration, production rate optimization, and reservoir recovery [1]. Pressure sensors designed for downhole applications require high operating temperature, large dynamic range, long telemetry distance, and low drift over long time.

Fiber optic sensors are competitive candidates for downhole pressure sensing because of their advantages of miniature in size, electromagnetic interference (EMI) immunity, high sensitivity, high-temperature resistance, and long reaching distance. Various optical fiber sensors have been proposed and successfully demonstrated for downhole pressure sensing, such as capillary encapsulated fiber extrinsic Fabry-Perot interferometric (EFPI) sensors [2]–[4], high birefringence fiber based Sagnac interferometer sensors [5], [6], Fiber Bragg

grating (FBG) based temperature and pressure sensors [7], [8], and polarization modulation based high birefringence fiber sensors [9]. Because the optical fiber serves as both the sensing unit and the telemetry channel, one of the challenges for the fiber optic sensor is to minimize the temperature-pressure cross-sensitivity and reduce the long-time drift. Several methods have been reported to compensate for the temperature influence by employing an in-line FBG sensor [1], [2] or using Raman scattering-based distributed sensors [4] for temperature compensation.

Recently, we proposed a passive digital sensing method, in which a rotary encoder was connected to a bimetallic coil to locally convert the analog temperature to a digital binary code [10]. As such, the data can be directly sent out in a digital format without using an analog-to-digital converter. By implementing this digital sensing approach to the downhole pressure sensor, the optical fiber is used merely as a telemetry channel to transmit the digital signals rather than an active sensing
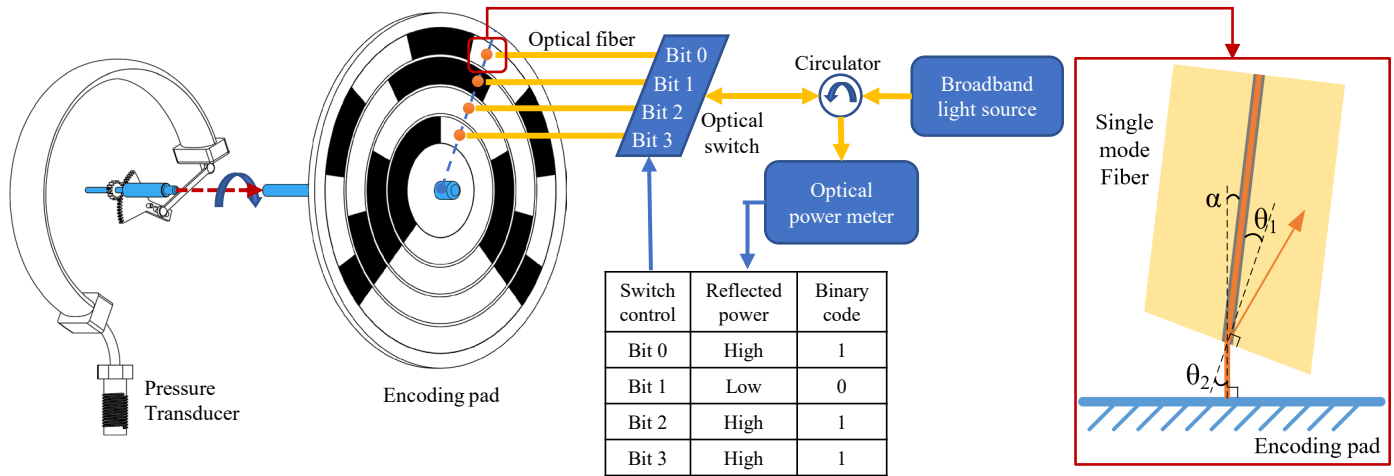
Fig. 1. Operational principle of optical encoder based downhole pressure sensor. A Bourdon tube transduces the pressure to the rotation angle. The optical encoder transform the rotation angle into binary code. The black region on the encoding pad represents the low reflectivity region, while the white region has high reflectivity. Enlarged figure on the right: Optical path at fiber tip. The fiber end was polished to have an inclination angle of θ_1.

element. Therefore, the environmental variations (e.g., temperature and strain) caused long-term drifts of the optical fiber become negligible. Furthermore, compared to the analog signal, the nature of high signal-to-noise ratio (SNR) of the digital signal makes it suitable for long-distance telemetry.

Another challenge for optical fiber sensors is to develop a suitable packaging technique that can bond the fiber to the transducer and protect the fragile fiber from breaking. Traditional methods, including using high-temperature epoxy or ceramic adhesive, have the problem of thermal expansion mismatching. This could lead to a large signal drift or even structural failure at an elevated temperature. Fused silica, which has similar material properties to the optical fiber, becomes an ideal choice for fabricating the fiber optic sensor's packaging structures. Recently, glass additive manufacturing utilizing the direct laser melting method has been demonstrated [11]. By integrating the picosecond laser-based subtractive manufacturing technique, the machining system offers great flexibility and simplicity to produce desired 3D structures with no post-treatment and high-temperature resistance. Various all-glass FPI sensors have been fabricated using this glass additive and subtractive manufacturing (ASM) system for temperature [12] and pressure [13], [14] sensing.

In this paper, the environmental pressure is first transduced by a Bourdon tube to the rotation angle, which is then mechanically sampled by an optical rotary encoder as binary digital codes. The rotary encoder is composed of an encoding pad and an optical fiber sensing head. The stainless-steel encoding pad is fabricated by the picosecond laser blackening technique [15], [16]. The high fabrication precision of the picosecond laser enables micrometer-level code writing. The ASM system is employed to embed optical fibers into a bulk fused silica glass to interrogate the encoding pad. The picosecond laser is used to fabricate the optical fiber embedded channels. Glass 3D printing technique is then used to seal the sensing fiber inside the channels. The integrated all-glass sensing head is finished by polishing the fiber end face to a designed inclination angle to minimize the end face reflection. The SNR, pressure response, and long-term drift of the fabricated prototype sensor will be experimentally examined.

II. OPERATIONAL PRINCIPLE

As shown in Fig. 1, the proposed pressure sensor consists of three parts: a Bourdon tube pressure transducer, an encoding pad, and a fiber optic interrogation system. Given different pressure, the Bourdon tube generates different rotation angles. The encoding pad, which connects to the center shaft of the Bourdon tube, will rotate accordingly. The Gray coding is used to code the upper 3/4 part of the pad. The black area has low reflectivity, while the white area has high reflectivity. Four optical fibers embedded in the all-glass sensing head are aligned to four encoding channels, accordingly. A broadband light source is used to prevent light interference. The laser light passes through a circulator to an optical fiber switch. The optical switch connects to the optical fiber sensing head. The light is then reflected back from the encoding pad. The reflected light transmits through the optical switch and the circulator, and is received by an optical power meter. If the sensing head is pointed to the high reflection area (white area), we will receive high reflected power, which corresponds to the digital state "1". If the sensing head is pointed to the low reflection area (black), we will receive low reflected power, which corresponds to the digital state "0". For example, as showing in Fig. 1, this rotation angle corresponds to a binary code of "1101".

To obtain high SNR, we need to increase the light intensity difference between digital states "1" and "0". The received light comprises the light reflected from the encoding pad and the optical fiber end face. Therefore, we need to increase the reflectivity contrast of the encoding pad and minimize the light intensity reflected from the fiber end face. The enlarged figure in Fig. 1 shows the diagram of optical path at the fiber tip. The fiber tip is polished to have an inclination angle of θ_1. The angle of the refracted light, which is the light emitted into the air, can be calculated using Snell's law,

$$\theta_2 = \sin^{-1}\left(\frac{n_{fiber}}{n_{air}} \sin\theta_1 \right), \tag{1}$$

where n_{fiber} is the refractive index of optical fiber and n_{air} is the refractive index of air. In order to have the light vertically
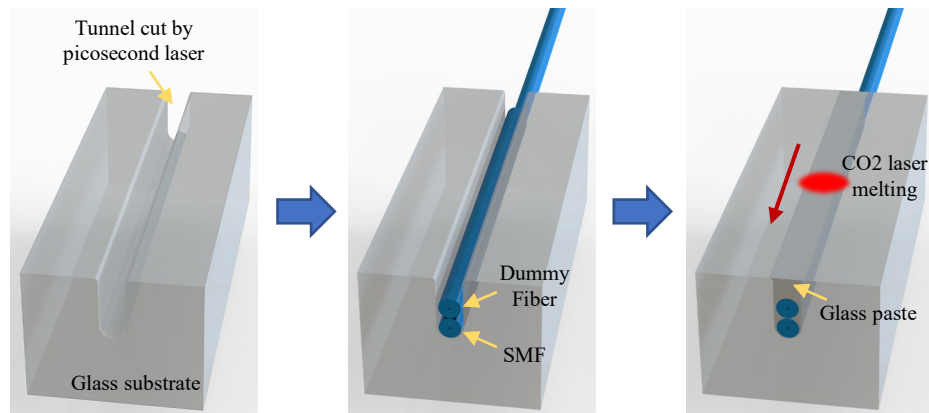
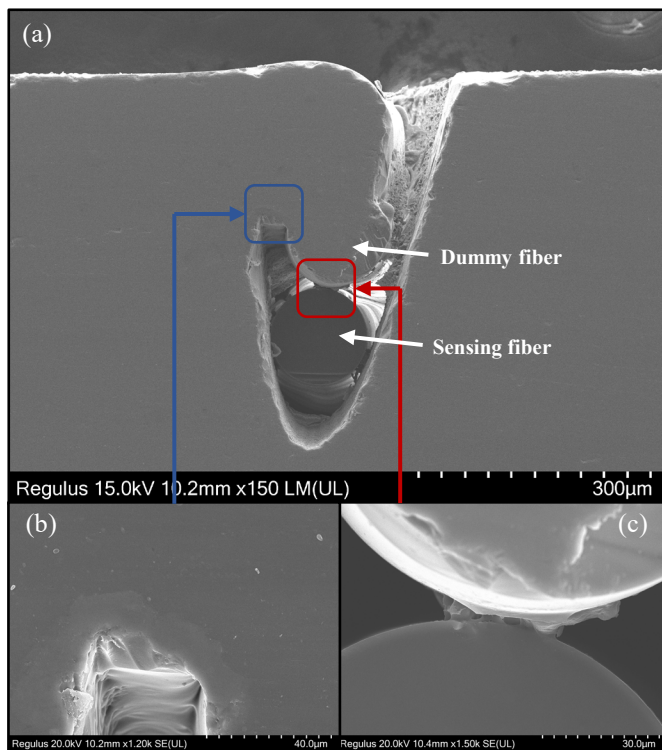Fig. 2. Procedure of packaging the sensing fiber into a bulk fused silica glass.

Fig. 3. SEM image of the polished cross-section viewed 3D printed all-glass fiber head. (a) Overview. (b) Connection between the substate and the glass paste. (c) interface between the dummy fiber and the sensing fiber.

emitting to the encoding pad, the optical fiber should have an inclination angle of

$$\alpha = \theta_2 - \theta_1. \qquad (2)$$

III. SENSOR MANUFACTURING

A. Optical fiber embedded all-glass sensing head

To realize the design shown in Fig 1, we plan to seal the optical fiber in a fused silica substrate using glass ASM techniques. And then polish the bulk all-glass sensing head to the designed angles.

The manufacturing system is mainly composed of a CO2 laser (Firestar ti100, SYNRAD Inc., with a wavelength of 1064 nm), a ps laser (APL-4000-1064, ATTODYNE Inc., with a wavelength of 1064 nm and a pulse width of 5 ps), and a paste dispersion system [11], [17]. The fabrication procedure is
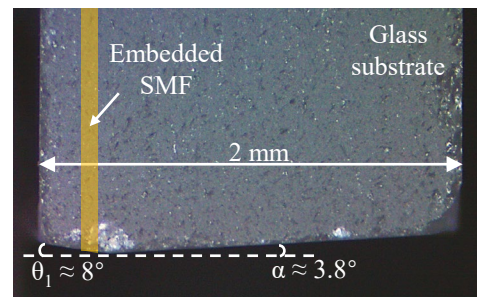

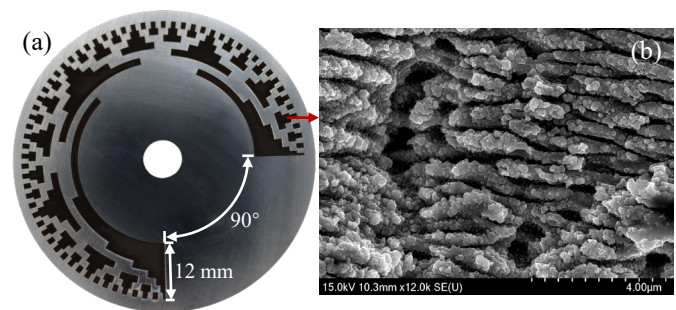Fig. 4. Side view of the polished all-glass sensing head.

Fig. 5. (a) Polished stainless-steel disc coded using picosecond laser. (b) SEM image of the blackened region.

TABLE I
PROCESSING PARAMETERS FOR ADDITIVE AND SUBTRACTIVE MANUFACTURING

Parameters	Glass substrate cutting	Glass paste melting	Stainless-steel laser blackening
Laser type	Ps laser	CO2 laser	Ps laser
Laser power	4W	10W	1.6W
Laser pulse repetition frequency	200kHz	-	100kHz
Laser spot scanning speed	300 mm/s	0.5 mm/s	15 mm/s
Hatching line spacing	0.025 mm	-	0.015 mm

shown in Fig. 2. The fused silica glass substrate is first cut by the ps laser with the processing parameters shown in Table 1. Two single mode fibers (SMFs) are vertically placed inside the tunnel. The glass pastes [11] are extruded on top of the fiber through an extruder (eco-Pen300, Preeflow). The excess paste is then manually removed through a blade. CO_2 laser irradiation is conducted with optimized output power, scanning speed, and spot size to melt the glass paste with the substrate to seal the sensing fiber [12].

The fabricated tunnel has a width of 0.3 mm and a depth of 0.5 mm. The tunnel width is smaller than the CO2 laser spot size (about 0.5-mm-diameter), so that the laser can melt the glass paste and the substrate simultaneously to obtain better bonding results. The depth of the tunnel is large enough to bury two SMFs and prevent the sensing fiber from being melted. The dummy fiber, placed on top of the sensing fiber, is used to provide extra protection for the sensing fiber [17]. In addition, because the melting depth of the glass paste is influenced by laser power and scanning speed, the existence of dummy fiber also released the control requirements of the CO_2 laser parameters.

Fig. 3 shows the polished cross-section view of the all-glass sensing head. The dummy fiber was melted with the glass substrate without micro crack. The dummy fiber and the added glass paste created a shield to secure the sensing fiber. The sensing fiber remains intact, which can be seen at the interface between the dummy fiber and the sensing fiber.

After the optical fiber was sealed inside the glass substrate, we polished the fiber end surface. Two 3D-printed plastic polishing holders are fabricated to fix the sensing head to the designed angle of $\theta_1 = 8°$ and $\alpha = 3.8°$ based on equations (1) and (2). Here we choose the fiber tip angle equal to 8°, which is similar to the FC/APC optical fiber connector. As such, an expected return loss should be around -60dB. The polished result is shown in Fig. 4. The encoding pad should be placed parallel to the 3.8° polished surface.

B. Encoding pad

The encoding pad is made of stainless steel. An 8-bit Gray code is fabricated using the ps laser blackening technique [15], [16]. The processing parameters are shown in Table 1. Fig. 5(a) shows the fabricated encoding pad. The whole encoding area occupied 270° with a single bit number corresponding to 270/256 = 1.0547°. Each encoding channel has a width of 1.5 mm. The outer diameter of the encoding area is 60 mm. Fig. 5(b) is the SEM image of the laser blackened region. Generated ripples and valleys in the sub-micro scale increase the surface roughness and reduce the amount of light reflected back to the same angle as the incident direction.
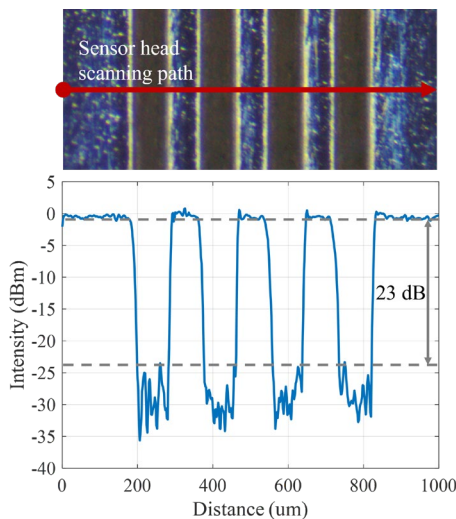
IV. EXPERIMENTS

We conducted three experiments to demonstrate the proposed pressure sensor and verify its performances, including the SNR, pressure response, and long-time stability. We used a lightwave multimeter (Agilent 8163A with HP 81533B optical head interface) as the optical receiver. A broadband laser (BBS 1550 A-TS, AFC TECHNOLOGIES Inc.) was used as the light source. The emitted light has a center wavelength of 1550 nm and a bandwidth of about 50 nm. The estimated coherent length is 15.3 um. The distance between the fiber end face and the encoding pad is about 200 um. As such, the light reflected from the fiber end face won't interfere with the light reflected from the encoding pad. The maximum value of the distance between the fiber end face and the pad is restricted by the loss of optical interrogation system and the detection limited of the optical power meter. As the distance increases, the emitted beam size will increase, so that the light intensities will decrease. If the loss of optical interrogation system (e.g., long telemetry distance, aging of optical devices, or hydrogen darkening of optical fiber) becomes larger, the reflected light intensity of the blackened region could be lower than the detection limit of the optical power meter. As such, the SNR will decrease. In this case, additional power amplifiers or an optical receiver with higher sensitivity needs to be implemented to increase the SNR.

A. SNR

The proposed sensing system is first demonstrated by a single bit channel test. Four rectangular areas with a width of 100 um and an interval of 80 um were laser blackened using the same laser parameter listed in Table 1. The microscope picture of the pad is shown in Fig. 6(a). The optical fiber sensing head was fixed on a motorized stage with an inclination angle of 3.8°. The sensing head scanned across the pad with a speed of 0.01 mm/s, while the optical power meter recorded the readings with a sampling period of 0.2s. The test results are shown in Fig. 6(b). When the sensing head moved on top of the un-blackened area, we received high reflected light intensities larger than -1 dBm.

(a)   (b)

(c)

Fig. 6. SNR test results. The optical fiber sensor head was scanning through four evenly distributed blackened region.
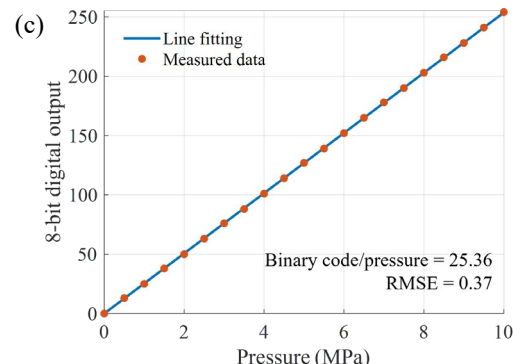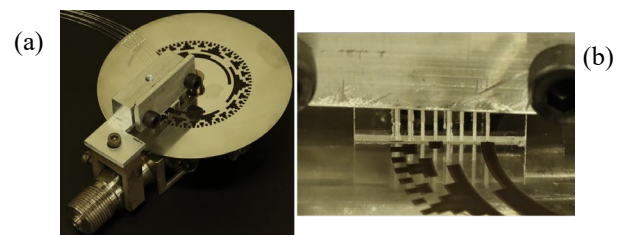
Fig. 7. (a) Assembled pressure sensor. (b) Alignment between the optical fiber head and the encoding pad. (c) Pressure response test results.

When the sensing head moved on top of the blackened area, we received low reflected light intensities smaller than -24 dBm. Therefore, the system's SNR is around 23 dB. The average transition length, which is the distance from 10% to 90% of -1 dBm light intensities, is about 8.5 um.

B. Pressure Response

Fig. 7(a) shows the assembled pressure sensor. A commercially available Bourdon tube with a measurement range of 10MPa was assembled with the encoding pad and the sensing head. Fig. 7(b) shows the detailed view of the sensing head aligned to the encoding pad. A 1x8 bidirectional optical fiber switch was used to multiplex the eight sensing fibers. A deadweight tester (1305D, ASHCROFT) with a reference sensor (700G31, FLUKE) was used to test the proposed pressure sensor. Pressure ranged from 0 MPa (atmospheric pressure) to 10 MPa with an incremental of 0.5 MPa was applied to the developed sensor. The measured data has a root-mean-square error (RMSE) of 0.37. In addition, there were no erroneous readings between the digital state "0" and "1".

C. Long-Term Stability Test

The pressure sensor was placed inside the temperature chamber (DX 300, Yamato) to test its long-time drift at high temperature environment. Fig. 8 shows the test results of the optical encoder's last significant bit (LSB). The pressure sensor was tested at 250°C for 400 hours. At the beginning of the test, the received light intensity experienced a 1.5 dBm fluctuation. Because the temperature is rapidly increased from room temperature to 250°C, the sensor head fixing structure could have a small distortion caused by the thermal expansion. The received light intensity tends to go back to its original value during the test. After being tested for about 250 hours, the reflected light gradually reduced. This could be caused by the oxidation of the encoding pad. The oxidation layer might deteriorate the encoding pad's surface reflectivity. However, the intensity fluctuations during the entire test are relatively small compared to the SNR. And the digital output code did not change during the 400-hour-test.

This long-time intensity fluctuations can be reduced by applying a layer of protective coating (e.g., gold coating) on the encoding pad. Because the coated material also can be ablated by the ps laser with high precision [18], we can use a similar
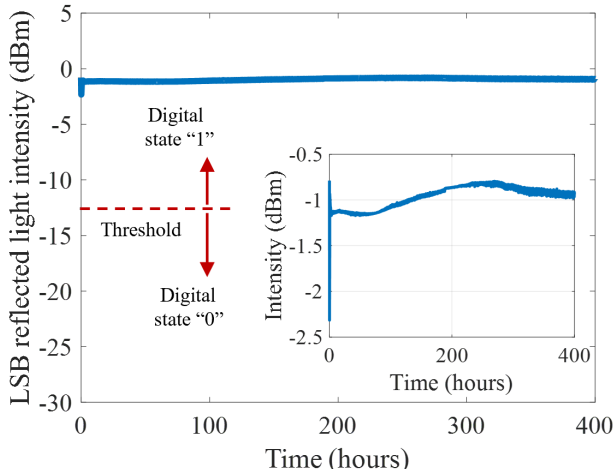

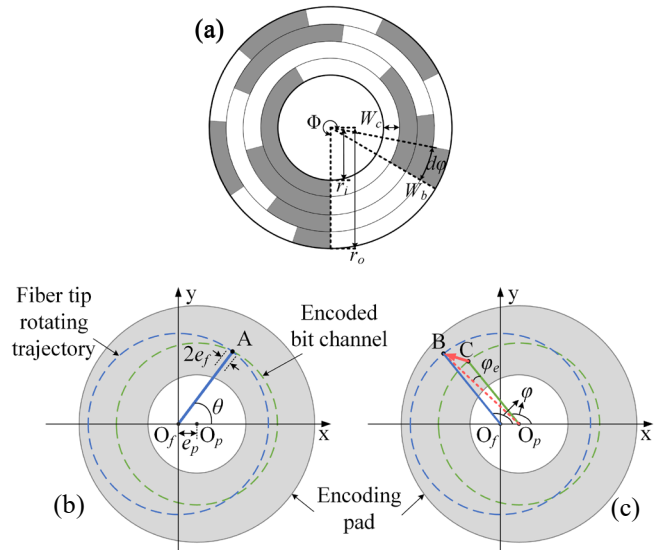
Fig. 8. Pressure sensor test at 250°C for 400 hours.

Fig. 9. (a) Schematic of the encoding pad. (b) Initial alignment state. The fiber tip (blue solid line) is aligned to the encoding pad at point A. (b) Testing state. When the fiber tip rotates to point B, a misalignment angle of φ_e is generated. Φ, angles of the full encoded region; $d\varphi$, angles of a single bit; r_i, inner radius of the encoding pad; r_o, outer radius of the encoding pad; W_c, bit channel width; W_b, minimum arc length of a single bit; O_f, rotation center and coordinate origin; O_p, encoding pad center; θ, initial alignment angle between fiber head and encoding pad; φ, rotation angle; e_f, the maximum misaligned distance at fiber tips; e_p, the misaligned distance between the rotation center and encoding pad center.

method to fabricate the encoding pad. Moreover, the gold coating could improve the reflectivity of the pad, which can further improve the sensor's SNR.

V. Discussion

A prototype sensor has been demonstrated to prove the feasibility of the proposed sensing method. However, the sensor's performances, such as size and resolution, have not reached to their limitations. Here, we will establish a mathematical model to study the relationships between the sensor's performances and the design parameters, and evaluate the tradeoffs between the rotary encoder's size and resolution.

The schematic of the encoding pad and the relationship between the pad and fiber head are shown in Fig. 9. Five boundary conditions need to be satisfied in designing the rotary encoder. First, the misaligned angle between the fiber head and encoding pad, φ_e, should be limited within the range of a single-bit code, $d\varphi$, so there will be no erroneous digital outputs. Second, the overall encoding angle, Φ, should be smaller than 2π. Third, the bit channel width, W_c, is equal to the interval of fiber tips. And the fiber tips need to have a separation distance that is larger than the CO_2 laser spot size, W_L. As such, W_c should be larger than W_L. Fourth, the minimum arc length of a single-bit code, W_b, should be larger than the transition length, W_T. Fifth, the outer radius, r_o, should be large enough to encode n-bit codes. So that we have

$$\begin{cases} d\varphi \geq |\varphi_e| S_e \\ 0 < \Phi = d\varphi \cdot 2^n \leq 2\pi \\ W_c \geq W_L S_L \\ W_b = d\varphi(r_0 - W_c) \geq W_T S_T \\ r_0 \geq n W_c \end{cases}, \qquad (3)$$

where S_e, S_L, and S_T are the safety factors.

First, we will calculate φ_e. As shown in Fig. 9(b), there are two misalignments, including e_p, the distance between the encoding pad center and the rotation center, and e_f, the maximum misaligned distance at fiber tips. Because the bit channel width is much larger than the misaligned distance, we assume the fiber tip will not move to the other bit channels. Hence, we ignore the misalignment in the radial direction. θ is the initial alignment angle between the fiber head and the pad. Different θ represents different relative positions between the fiber head and encoding pad.

As shown in Fig. 9(c), when the fiber head rotates to an angle of φ, it should contact the encoding pad at point C, which is at the location of

$$(X_C, Y_C) = (r\cos(\varphi) + e_p, r\sin(\varphi)), \qquad (4)$$

where r is the radius of the encoded bit channel (green dash circle). However, due to the misalignment, the real location of the fiber head is at point B, which can be expressed as

$$(X_B, Y_B) = \left(R(\theta)\cos\left(\varphi \pm \frac{e_f}{R(\theta)}\right), R\sin\left(\varphi \pm \frac{e_f}{R(\theta)}\right) \right), \qquad (5)$$

where R is the radius of the fiber head rotating trajectory (blue dash circle). Because the arc length of φ_e is much smaller than the radius $(\varphi_e r \ll r)$, φ_e can be approximated as the tangential projection of vector $\overline{CB}$ at point C. Therefore,

$$\varphi_e \approx \frac{\overline{CB} \cdot \overline{I_C}}{r} = \frac{e_p \sin(\varphi) + R(\theta)\sin\left(\pm \dfrac{e_f}{R(\theta)}\right)}{r}, \qquad (6)$$

where $\overline{I_C} = (\cos(\varphi + \pi/2), \sin(\varphi + \pi/2))$ is the unit tangent vector at point C. Because $e_f \ll R(\theta)$, we have $\sin(e_f/R(\theta)) \approx e_f/R(\theta)$. As such

$$\varphi_e \approx \frac{e_p \sin(\varphi) \pm e_f}{r}. \qquad (7)$$

According to Equation (7), φ_e is negatively proportional to the encoding radius, r. And θ has an ignorable influence on φ_e if the approximation conditions are valid. The maximum absolute value of φ_e should be obtained when $r = r_i$ and $\varphi = 90°$ or $180°$. By simplifying Equation (3) and substituting Equation (7), we have
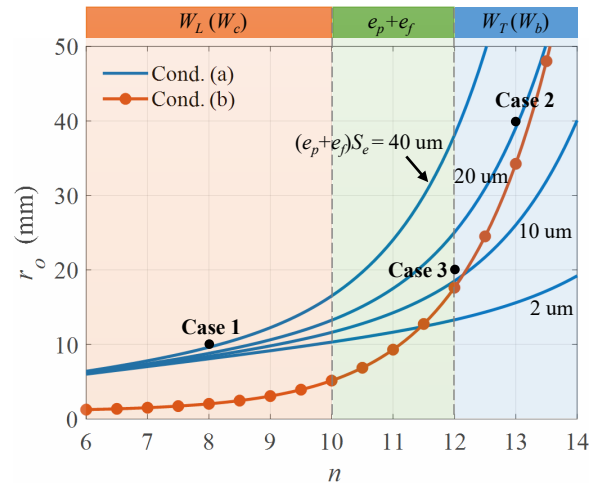

Fig. 10. Relationship between encoding pad outer radius, r_o, and the number of encoded bits, n, at $(e_p+e_f)S_e$ equals to 2 um, 10 um, 20 um, and 40 um.

$$\begin{cases} r_o \geq \dfrac{(e_p + e_f)S_e}{\Phi} 2^n + W_L S_L n, & \text{Cond.(a)} \\ \\ r_o \geq \dfrac{W_T S_T}{\Phi} 2^n + W_L S_L, & \text{Cond.(b)} \\ \\ 0 < \Phi \leq 2\pi, & \text{Cond.(c)} \end{cases} \qquad (8)$$

From the experiment results, we have $W_T = 8.5$ um and $W_L = 500$ um. Given $\Phi = 2\pi$, $S_L = 2$, and $S_T = 3$, the relationship between r_o and n at different $(e_p+e_f)S_e$ is shown in Fig. 10. The achievable performances combination of r_o and n are located at the region above the condition curves (a) and (b). Obtaining smaller size and higher resolution are a tradeoff in the proposed sensor designs. As for the applications that require small size ($r_o \leq 10$ mm), the sensor's performances are mainly determined by the term, $W_L S_L n$, in Cond. (a). The requirements for alignment accuracy and transition area length are relatively low. The minimum size of the encoder is mainly determined by the minimum achievable bit channel width, W_c. In the proposed system, W_c is mainly limited by the CO_2 laser spot size, W_L. Case 1 is a typical point in this region, where $n = 8$ and $r_o = 10$ mm can be achieved with $(e_p+e_f)S_e = 40$ um. As for the applications that require high resolution $(n \geq 12)$, the exponential term, $\dfrac{W_T S_T}{\Phi} 2^n$, dominates the tradeoff between r_o and n. The requirement for bit channel width is released. Considering current system settings, reducing the transition area length, W_T, is an efficient way to achieve high resolution in a relatively small size. Case 2 is a typical point in this region, where $n = 13$ and $r_o = 40$ mm can be achieved with $(e_p+e_f)S_e = 20$ um. As for the application requires both small size and high resolution $(10 \leq n \leq 12)$, the sensor's performances are mainly determined by the exponential term, $\dfrac{(e_p + e_f)S_e}{\Phi} 2^n$. The alignment accuracy has the most important influence on the sensor's performance. Case 3 is a balanced decision-making

point to obtain high resolution ($n = 12$) and small size ($r_o = 20$ mm) simultaneously.

VI. Conclusion

This paper presented a fiber optic rotary encoder-based pressure sensor for downhole applications. A glass additive and subtractive manufacturing system was used to fabricate the optical fiber sensing head and encoding pad with high accuracy. The prototype sensor has an SNR of 23 dB and a linear pressure response with an RMSE of 0.37. During the 400-hour high-temperature (250°C) test, the sensor's digital readings remain the same. The reflected light intensity has a small fluctuation of about 1.5 dBm, which is ignorable compared to the digital state changing threshold. According to the mathematic model between design parameters and sensor performances, the pressure sensitivity of $1/2^{12} \times 100\% = 0.02\%$ can be achieved with an outer radius of 20 mm. The features of high SNR, low drift, and high working temperature make the proposed sensing system suitable for downhole applications. Corporate with other types of transducers, like temperature or displacement, the sensing system can also be used to measure different physical quantities in harsh environments.

References

[1]   X. Zhou, Q. Yu, and W. Peng, "Fiber-optic Fabry–Perot pressure sensor for down-hole application," *Opt. Lasers Eng.*, vol. 121, pp. 289–299, 2019.

[2]   Q. Zhao *et al.*, "Adhesive-free bonding fiber optic Fabry–Perot pressure sensor based on oxy-hydrogen flame welding and spiral tube," *Opt. Commun.*, vol. 476, p. 126307, 2020.

[3]   S. H. Aref, M. I. Zibaii, and H. Latifi, "An improved fiber optic pressure and temperature sensor for downhole application," *Meas. Sci. Technol.*, vol. 20, no. 3, p. 34009, 2009.

[4]   K. Chen, X. Zhou, B. Yang, W. Peng, and Q. Yu, "A hybrid fiber-optic sensing system for down-hole pressure and distributed temperature measurements," *Opt. Laser Technol.*, vol. 73, pp. 82–87, 2015.

[5]   H. Y. Fu *et al.*, "High pressure sensor based on photonic crystal fiber for downhole application," *Appl. Opt.*, vol. 49, no. 14, pp. 2639–2643, 2010.

[6]   Z. Liu, L. Htein, K.-K. Lee, K.-T. Lau, and H.-Y. Tam, "Large dynamic range pressure sensor based on two semicircle-holes microstructured fiber," *Sci. Rep.*, vol. 8, no. 1, pp. 1–9, 2018.

[7]   P. M. Nellen *et al.*, "Reliability of fiber Bragg grating based sensors for downhole applications," *Sensors Actuators A Phys.*, vol. 103, no. 3, pp. 364–376, 2003.

[8]   J. Wang, X. Fu, H. Gao, X. Gui, H. Wang, and Z. Li, "FPGA-Based Dynamic Wavelength Interrogation System for Thousands of Identical FBG Sensors," in *Photonics*, 2022, vol. 9, no. 2, p. 79.

[9]   X. Li, H. Zhang, C. Qian, Y. Ou, R. Shen, and H. Xiao, "A new type of structure of optical fiber pressure sensor based on polarization modulation," *Opt. Lasers Eng.*, vol. 130, p. 106095, 2020.

[10]   W. Zhu *et al.*, "Passive digital sensing method and its implementation on passive RFID temperature sensors," *IEEE Sens. J.*, vol. 21, no. 4, pp. 4793–4800, 2020.

[11]   J. Lei, Y. Hong, Q. Zhang, F. Peng, and H. Xiao, "Additive manufacturing of fused silica glass using direct laser melting," in *CLEO: Applications and Technology*, 2019, pp. AW3I-4.

[12]   Q. Zhang *et al.*, "Information integrated glass module fabricated by integrated additive and subtractive manufacturing," *Opt. Lett.*, vol. 45, no. 7, pp. 1663–1666, 2020.

[13]   Q. Zhang, J. Lei, Y. Chen, Y. Wu, C. Chen, and H. Xiao, "3D printing of all-glass fiber-optic pressure sensor for high temperature applications," *IEEE Sens. J.*, vol. 19, no. 23, pp. 11242–11246, 2019.

[14]   Q. Zhang, J. Lei, Y. Chen, Y. Wu, and H. Xiao, "Glass 3D printing of microfluidic pressure sensor interrogated by fiber-optic refractometry," *IEEE Photonics Technol. Lett.*, vol. 32, no. 7, pp. 414–417, 2020.

[15]   H. Huang, L.-M. Yang, S. Bai, and J. Liu, "Blackening of metals using femtosecond fiber laser," *Appl. Opt.*, vol. 54, no. 2, pp. 324–333, 2015.

[16]   B. Liu *et al.*, "Porous microstructures induced by picosecond laser scanning irradiation on stainless steel surface," *Opt. Lasers Eng.*, vol. 78, pp. 55–63, 2016.

[17]   J. Lei *et al.*, "Laser-assisted embedding of all-glass optical fiber sensors into bulk ceramics for high-temperature applications," *Opt. Laser Technol.*, vol. 128, p. 106223, 2020.

[18]   J. Lei *et al.*, "One-Step Fabrication of Nanocrystalline Nanonetwork SnO2 Gas Sensors by Integrated Multilaser Processing," *Adv. Mater. Technol.*, vol. 5, no. 8, p. 2000281, 2020.